

Radiation-induced defect accumulation and annealing in Si-implanted gallium oxide

S.B. Kjeldby¹, A. Azarov¹, P.D. Nguyen¹, V. Venkatachalapathy^{1,2}, R. Mikšová³,
A. Macková^{3,4}, A. Kuznetsov¹, Ø. Prytz¹, and L. Vines¹

1) Department of Physics and Center for Materials Science and Nanotechnology, University of Oslo, Oslo, Norway

2) Department of Materials Science, National Research Nuclear University, “MEPhI”, Moscow, Russian Federation

3) Nuclear Physics Institute of the Czech Academy of Sciences, Řež, Czech Republic

4) Department of Physics, Faculty of Science, J.E. Purkyně University, Ústí nad Labem, Czech Republic

Defect accumulation and annealing phenomena in Si-implanted monoclinic gallium oxide (β -Ga₂O₃) wafers, having ($\bar{2}01$), (010), and (001) orientations, were studied by Rutherford backscattering spectrometry in channeling mode (RBS/c), X-ray diffraction (XRD), and (scanning) transmission electron microscopy ((S)TEM). Initially, the samples with different surface orientations were implanted with 300 keV ²⁸Si⁺-ions, applying fluences in the range of 1×10^{14} - 2×10^{16} Si/cm², unveiling interesting disorder accumulation kinetics. In particular, the RBS/c, XRD, and (S)TEM data combined, suggested that the radiation disorder buildup in Si-implanted β -Ga₂O₃ is accompanied by significant strain accumulation, assisting crystalline-to-crystalline phase transitions instead of amorphization. Selected samples having ($\bar{2}01$) orientation were subjected to isochronal (30 min) anneals in the range of 300 - 1300 °C in air. Systematic RBS/c and XRD characterization of these samples suggested complex structural transformations, which occurred as a function of the fluence and the temperature. Moreover, a detailed (S)TEM analysis of the sample implanted with 2×10^{16} Si/cm² and annealed at 1100 °C was enhanced by applying dispersive X-ray and electron energy loss spectroscopies. The analysis revealed silicon agglomerations in the form of silicon dioxide particles. Signal from silicon was also detected outside of the agglomerates, likely occurring as substitutional Si on Ga sites.

1. Introduction

Gallium oxide (Ga₂O₃) is a modern ultra-wide bandgap semiconductor of both academic and technological interest. On the technological side, Ga₂O₃ may provide unique opportunities to realize high-voltage tolerating devices as well as deep UV-operating optoelectronic devices. On the academic side, Ga₂O₃ shows rich variations in crystal structure through its polymorphism. In addition to the monoclinic β -phase (β -Ga₂O₃), which is the thermodynamically stable polymorph at room temperature and atmospheric pressure ¹, several other polymorphs including the orthorhombic κ -Ga₂O₃ ^{2,3}, the rhombohedral α -Ga₂O₃ ⁴, the spinel-like γ -Ga₂O₃ ⁵, and the bixbyite δ -Ga₂O₃ ^{6,7} were reported. The kinetics of annealing in gallium oxide and the related polymorph transformations have previously been investigated down to the atomic scale, particularly for transformations between κ - and β -phases ^{8,9}. The literature also contains atomic resolution studies of different Ga₂O₃ polymorphs grown by heteroepitaxy ^{10,11}.

Among the electronic dopants in β -Ga₂O₃, silicon (Si) is highly technologically important because it creates an efficient donor state by Si substituting for Ga in the crystal lattice ^{12,13}. Si occurs as an unintentional impurity in bulk β -Ga₂O₃ in concentrations up to 10^{16} - 10^{18} Si/cm³ ¹⁴, but can also be incorporated via in-diffusion or ion implantation ¹⁵. Ion implantation is often technologically preferable as it typically permits higher dopant localization control. β -Ga₂O₃ MOSFETs already utilize Si-implanted channels, which has motivated studies of Si diffusion and redistribution in Si-implanted Ga₂O₃ with post-implantation anneals ¹⁶.

However, systematic studies of the Si-ion induced radiation disorder evolution during annealing are at least incomplete, even though the fundamentals of the radiation effects in $\beta\text{-Ga}_2\text{O}_3$ has attracted significant interest in the research community¹⁷⁻²⁰. Very recently, Azarov et al.¹⁷ reported on phase transformation in $\beta\text{-Ga}_2\text{O}_3$ induced by Ni, Ga and Au ion-implantation. Ion-induced structural transformation in $\beta\text{-Ga}_2\text{O}_3$ has also been reported by Anber et al. for Ge-implantation²¹. This structural transformation may open up possibilities to alter the properties of single crystal wafers in a layer, or be used as a template for growth of other gallium oxide polymorphs.

Certainly, disorder accumulation and annealing phenomena must also be understood for Si-implanted $\beta\text{-Ga}_2\text{O}_3$, since Si-implantation is used in device fabrication. In the present work, we undertook a systematic investigation of the radiation-induced defect evolution in Si-implanted $\beta\text{-Ga}_2\text{O}_3$ wafers exhibiting different crystallographic orientations, in particular studying the effects of the implantation fluence and post-implantation anneals. Our results reveal a structural transformation for the highest fluences, and that significant disorder remains, even after annealing at 1100 °C. Moreover, annealing at 1100 °C revealed a significant amount of Si precipitates, likely in the form of SiO_2 , which may reduce the doping efficiency when used in devices.

2. Experimental procedures

Three types of $\beta\text{-Ga}_2\text{O}_3$ wafers with different surface orientations were used in this study: a bulk edge-defined film-fed grown (EFG) crystal wafer having $(\bar{2}01)$ surface orientation, a bulk EFG wafer having (010) surface orientation and a halide vapor phase epitaxy (HVPE) film with (001) orientation grown on a doped EFG substrate. All samples were obtained from Novel Crystal Technology Inc., with donor concentrations of 2.9×10^{17} , 2.2×10^{17} and $2.3 \times 10^{16} \text{ cm}^{-3}$ for the $(\bar{2}01)$, (010) and (001) wafers, respectively. Samples with a size of approximately $5 \times 5 \text{ mm}$ were cut from the wafers, and one sample from each orientation was left as an unimplanted reference without further processing. The samples were implanted with 300 keV $^{28}\text{Si}^+$ -ions applying a fluence range from 1×10^{14} to $2 \times 10^{16} \text{ Si/cm}^2$. The current density was kept constant at $1.7 \times 10^{13} \text{ ions/s cm}^2$ ($2.8 \mu\text{A/cm}^2$) for all implants to avoid dose-rate effects²⁰. All implants were performed at room temperature. Note that samples in the as-implanted state were too resistive for both electrical measurements and chemical profiling using e.g. secondary ion mass spectrometry. Hence, the ion depth profiles and the corresponding defect production were simulated using the SRIM code²², applying the density reported by Åhman et al. for $\beta\text{-Ga}_2\text{O}_3$ ²³. The $(\bar{2}01)$ -oriented samples were selected for a sequential 30-minute isochronal annealing series, at 300, 500, 700, 900, 1000, 1100, 1200 and 1300 °C in air.

Rutherford backscattering spectrometry in channeling mode (RBS/c) measurements were carried out using either 1.6 MeV or 2.0 MeV $^4\text{He}^+$ -ions in 165° and 170° backscattering geometry, respectively. Non-channeling (unaligned) RBS spectra were recorded for all samples. For these measurements, the sample was tilted away from channeling conditions. Under unaligned measurement conditions, the signal from crystalline and amorphous samples should be equivalent if the samples are otherwise identical. Therefore, unaligned RBS measurements represent an upper limit to the damage that the sample can accumulate during ion implantation, namely amorphization. Such RBS measurements are labeled as “random” below. Additionally, RBS/c spectra from as-received, unimplanted samples were recorded, which represent the limit of minimal sample damage. X-ray diffraction (XRD) characterization was performed using a Bruker AXS D8 Discover diffractometer with a monochromated Cu K_α X-ray source in locked couple mode.

Two $(\bar{2}01)$ -oriented samples implanted with $2 \times 10^{16} \text{ Si/cm}^2$ were prepared for (scanning) transmission electron microscopy ((S)TEM). One of the samples was annealed at 1100 °C for 30 minutes in air. The samples were prepared for cross-sectional observations by mechanical grinding and finished with Ar-ion milling in a Gatan Precision Ion Polishing System (PIPS II). (S)TEM imaging, selected area electron diffraction (SAD), energy dispersive x-ray spectroscopy (EDS) and electron energy-loss spectroscopy (EELS) measurements were done at 300 kV in a Cs-corrected Thermo Fisher Scientific Titan G2 60–300 kV microscope, equipped with a Gatan GIF Quantum 965 spectrometer, and Super-X EDS detectors.

3. Results and discussion

3.1 Role of the surface orientation

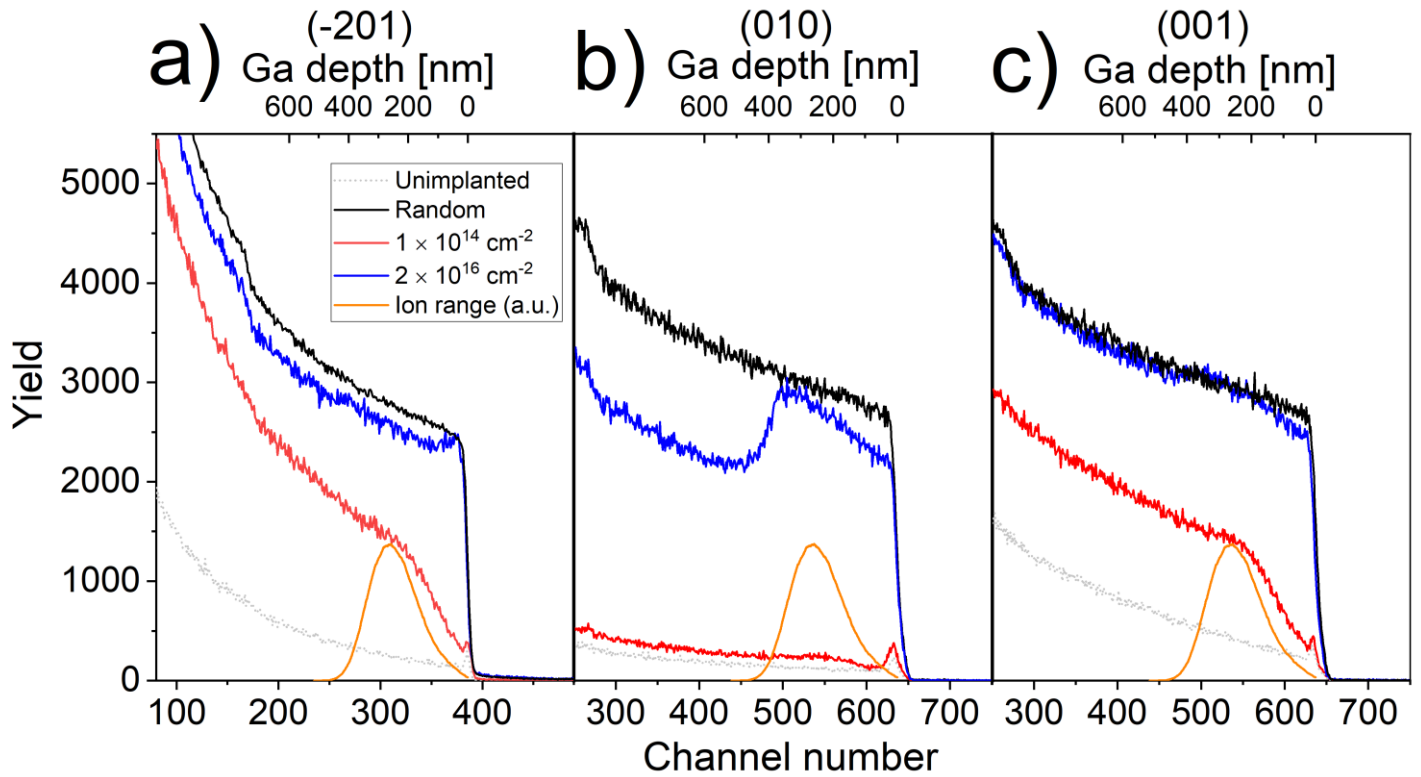


Figure 1 RBS/c spectra for a) $(\bar{2}01)$, b) (010) and c) (001) samples showing the effect of the surface orientation on implantation-induced defect accumulation in $\beta\text{-Ga}_2\text{O}_3$. (010) - and (001) -orientations were characterized with 2.0 MeV $^4\text{He}^+$ -ions, while the $(\bar{2}01)$ -orientation was characterized with 1.6 MeV $^4\text{He}^+$ -ions. Calculated depth scales for the Ga sublattice are given on top, and calculated Si-concentration profiles from SRIM have been included in orange (arbitrary units). The legend is shared across a), b) and c).

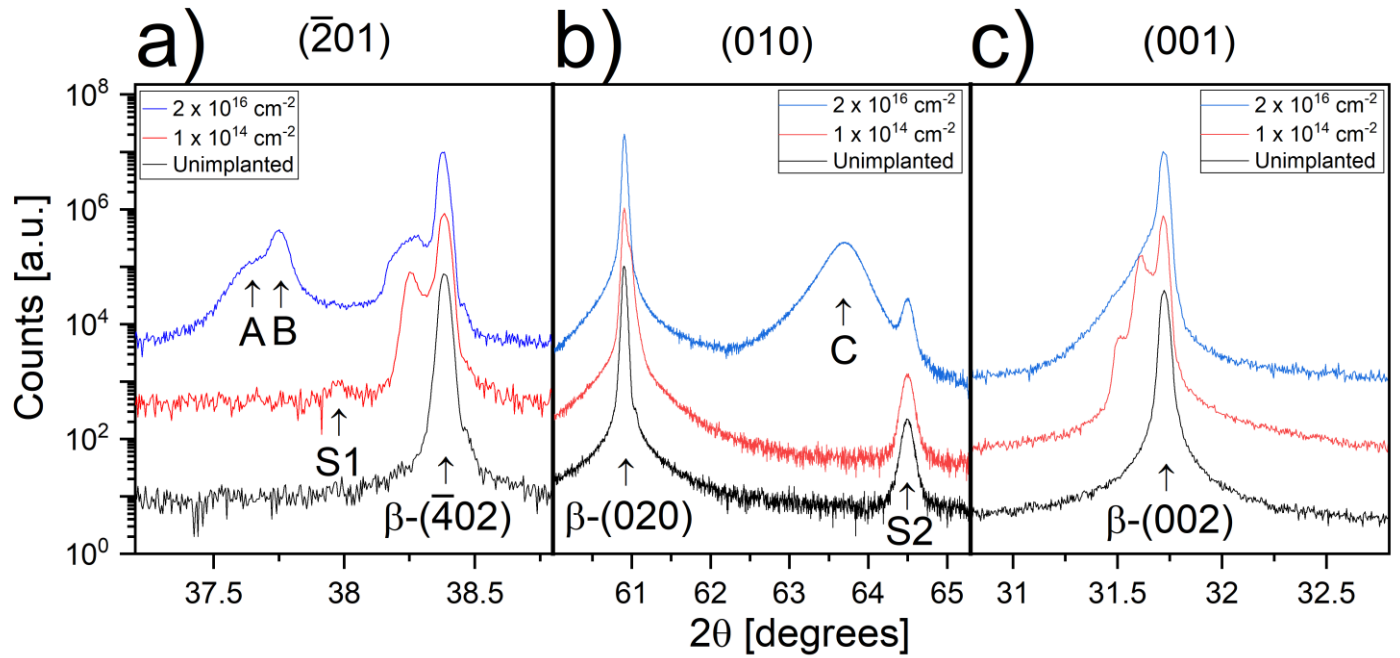


Figure 2 XRD diffractograms from samples with surface orientation a) $(\bar{2}01)$, b) (010) and c) (001) , for different implantation fluences. Uppercase letters A-C indicate additional diffraction peaks which appeared after implantation. Labels S1 and S2 indicate positions of known diffraction peaks from the sample stage.

Figure 1 shows RBS/c spectra of as-implanted $(\bar{2}01)$, (010) and (001) β - Ga_2O_3 samples in panels a), b) and c) respectively, comparing the data from the lowest (1×10^{14} Si/cm²) and highest (2×10^{16} Si/cm²) fluences with channeling spectra from the unimplanted samples. The spectra from the randomly oriented samples are also included in Figure 1. As described above, channeling measurements on unimplanted samples represent a lower limit to ion-induced damage accumulation, whereas “random” measurements represent the upper limit, namely amorphization. Note that the horizontal channel-number scale in Figure 1a) is different from that of Figure 1b) and c) because different He-ion energies were used. However, the calculated depth scales enable direct comparison of the spectra from the three different orientations. Additionally, calculated SRIM depth profiles²² of implanted atoms are plotted in Figure 1, revealing the implantation peak ~ 250 nm below the sample surface. The corresponding calculated vacancy profiles peaked at ~ 200 nm. Previous work in the literature has shown that SRIM calculations of the depth distribution for Si-implantation in β - Ga_2O_3 corresponds well with experimental measurements^{16,24}.

Different channels are active in RBS/c measurements on the differently oriented samples, which is corroborated by χ_{\min} -values of 4.1%, 3.8% and 7.4% for $(\bar{2}01)$ -, (010) - and (001) -oriented samples respectively, measured on the unimplanted samples. Although the former two orientations have similar χ_{\min} -values, it is clear from the rapid increase of the scattering yield at increased depth for $(\bar{2}01)$ that the probability of dechanneling is higher for this channel than for the active channel of (010) -oriented samples. The difference in He-ion energy is also partially responsible for the difference in dechanneling between $(\bar{2}01)$ - and (010) -oriented samples.

Naturally, disorder accumulation is observed in all samples independently of the surface orientation. This is evident from the fact that damage levels are increased for samples with higher implantation fluence. However, there are also distinct trends in the RBS/c spectra which depend on the surface orientation. This is likely caused by different defect types dominating in the corresponding channels or by a difference in the defect density and nature. To start with, both $(\bar{2}01)$ - and (001) -oriented samples showed high disorder for the fluence of 1×10^{14} Si/cm², whereas the (010) -oriented sample showed only slight deviation from the spectrum of the unimplanted sample. Moreover, a comparison between the dechanneling yields deeper in the samples indicates a significantly larger fraction of extended defects²⁵ for $(\bar{2}01)$ - and (001) -oriented samples compared with the (010) -oriented sample. Similar trends hold for samples implanted with 2×10^{16} Si/cm², i.e. $(\bar{2}01)$ - and (001) -oriented samples again exhibiting higher dechanneling in the bulk than the (010) -oriented

sample. Importantly, a prominent disorder plateau with a gradually increasing RBS/c yield extending to ~400 nm from the sample surface is observed in Figure 1b) for (010) surface orientation.

The (001)-oriented HVPE film and the unimplanted (010)- and ($\bar{2}01$)-oriented bulk samples may have had different defect concentrations prior to implantation. For implantation fluence 2×10^{16} Si/cm², the RBS/c yield was far larger than for the unimplanted samples for all orientations. Hence, the signal was dominated by ion-induced defects, and small variations in preexisting defect concentrations can safely be ignored. However, both for the (010)- and (001)-oriented samples, the RBS/c yield for fluence 1×10^{14} Si/cm² was much lower. Therefore, preexisting defects could contribute non-negligibly to the total defect concentration in these cases.

Figure 2 shows the XRD data from the same samples studied in Figure 1. In the ($\bar{2}01$)-oriented sample, ($\bar{2}01$), ($\bar{4}02$), ($\bar{6}03$) and ($\bar{8}04$) diffraction peaks were present in the diffractograms. Importantly, the emergence of additional diffraction peaks was observed around the ($\bar{4}02$) and ($\bar{8}04$) peaks. To show the evolution of these peaks, we have chosen to focus on the ($\bar{4}02$) peak at 38.39°, corresponding to a plane spacing of 2.343 Å. Calculated plane spacings from diffractograms are henceforth given in parenthesis. In the (010)- and (001)-oriented samples the main diffraction peaks were attributed to the (020)-planes at 60.90° (1.520 Å), and the (002)-planes at 31.71° (2.820 Å), respectively. In addition, diffraction peaks from the sample holder at 38.00° (2.366 Å) and 64.50° (1.444 Å) were detected.

For the 1×10^{14} Si/cm² implants, all samples showed an additional peak or shoulder on either the low-angle ((001)- and ($\bar{2}01$)-oriented) or high-angle ((010)-oriented) side of the main diffraction peak. These side peaks were attributed to the implantation-induced strain^{17,20}. The fact that tensile strain is observed for some crystal orientations and compressive strain is observed for others reveals anisotropy in the induced strain in the samples.

The 2×10^{16} Si/cm² implantation fluence was presumably high enough to reach the threshold reported by Azarov et al.¹⁷ and Anber et al.²¹ for structural transformation towards κ -Ga₂O₃. Indeed, a broad additional diffraction peak, labeled as peak C, appeared around 63.5° (1.46 Å) in the (010)-sample, and a double peak, labeled as peaks A and B, appeared around 37.5° (2.40 Å) in the ($\bar{2}01$)-sample for this fluence. In the (010) sample, the observed additional peak could be consistent with diffraction peaks from strained κ -Ga₂O₃ and is inconsistent with plane spacings in β -Ga₂O₃ from the literature²³. In the ($\bar{2}01$)-sample, the observed double peak could be attributed to strained κ -Ga₂O₃³, but could also be explained by strained β -Ga₂O₃, although the reported intensity ratios for the β -phase are not in good agreement with the observed intensity ratio from the double peak.

For the 2×10^{16} Si/cm² implants into the (001)-oriented sample, strain was observed as a broadening of the (002)-diffraction peak towards smaller angles. For this orientation, no additional diffraction peaks were observed. Note that our XRD measurements are only able to detect crystal planes lying parallel to the sample surface. Hence, it is possible that ion implantation causes additional diffraction peaks in this sample as well, but that these XRD peaks are invisible in our XRD geometry.

3.2 Defect annealing kinetics

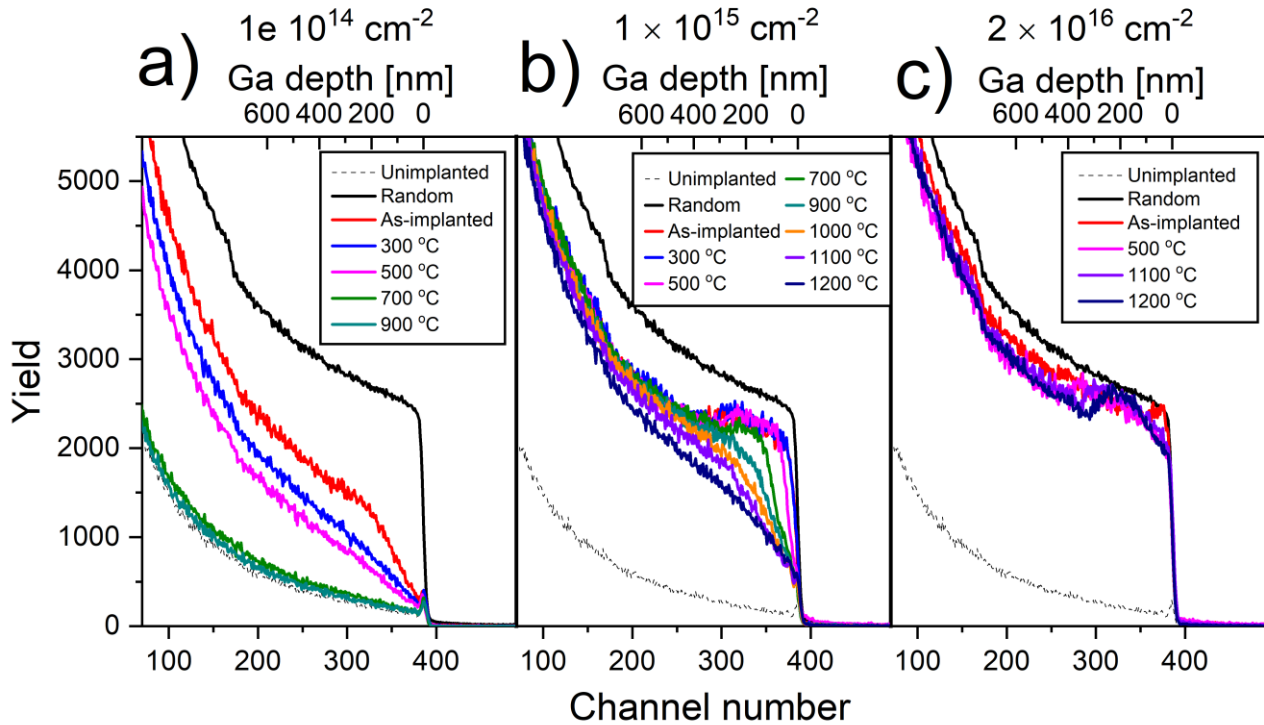


Figure 3 RBS/c spectra of $(\bar{2}01)$ -oriented samples subjected to a) 1×10^{14} Si/cm², b) 1×10^{15} Si/cm² and c) 2×10^{16} Si/cm² implants after implantation and after selected steps in the isochronal annealing series. The unimplanted (dotted gray line) and random (solid black line) spectra are shown for comparison. For the lowest fluence, the annealing series was terminated after 900 °C since defect levels had returned to those of the unimplanted sample.

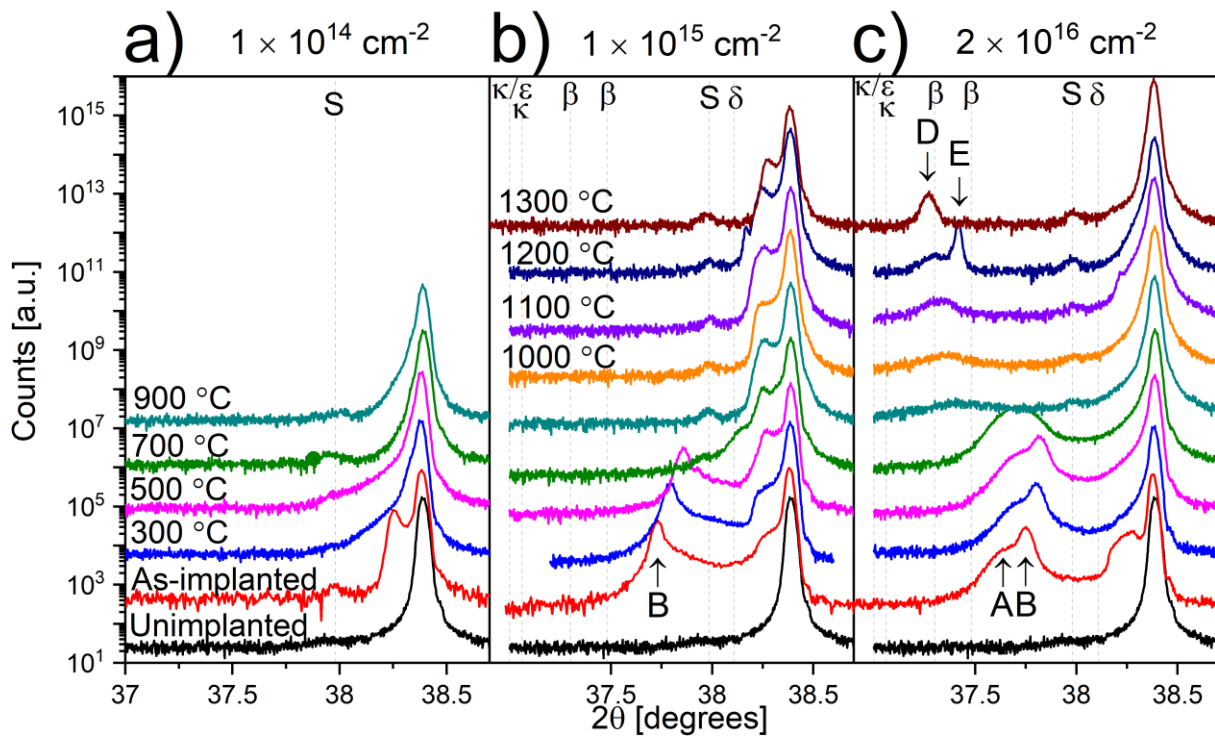


Figure 4 X-ray diffractograms from $(\bar{2}01)$ -oriented samples implanted to fluence a) 1×10^{14} Si/cm², b) 1×10^{15} Si/cm² and c) 2×10^{16} Si/cm². Uppercase letters A, B, D and E denote additional diffraction peaks which appeared after implantation or during the following annealing series. A

and B refer to the same peaks as in Figure 2a). Indicated plane spacings for Ga_2O_3 polymorphs (vertical gray dashed lines marked by phase) are taken from Åhman et al.²³, Cora et al.³ and Roy et al.⁷ for β -, κ - and δ -phase respectively. Vertical gray dashed lines marked with "S" are from the sample stage.

To investigate the annealing behavior of Si-implanted β - Ga_2O_3 , a 30-minute isochronal annealing study in air was undertaken for ($\bar{2}01$)-oriented samples, using RBS/c and XRD for sample characterization after each annealing step. Since the main feature of interest for XRD, appearance of additional diffraction peaks, was not observed for (001)-oriented samples in the surface orientation study, samples of this orientation were not included in the annealing study. Furthermore, some previous work exists in the literature on the annealing behavior of (010)-oriented samples¹⁷. Consequently, this orientation was also excluded from the annealing study. Finally, the significant technological interest in ($\bar{2}01$)-oriented samples justifies focusing on this sample orientation.

Figure 3 shows the RBS/c spectra from the annealing series of ($\bar{2}01$)-oriented samples implanted with 1×10^{14} , 1×10^{15} and 2×10^{16} Si/cm². The channeling spectrum from the unimplanted sample and the random spectrum are shown for comparison. Spectra with little change from the previous annealing step were excluded from Figure 3c).

Figure 3 reveals that the defect evolution exhibits prominent dependence on the fluence. Indeed, for the lowest implantation fluence (1×10^{14} Si/cm²), significant defect reduction occurred after annealing at 300 °C, with defect levels close to that of the unimplanted sample regained already at 700 °C. For the intermediate implantation fluence (1×10^{15} Si/cm²), a defect plateau was present within ~ 300 nm from the sample surface. Defect level reduction in this region started from the surface after annealing at 500 °C, with the defect plateau disappearing after 900 °C. However, high dechanneling yield behind the damage peak persisted and further heat treatments resulted in a minor backscattering yield reduction only. For the highest implantation fluence (2×10^{16} Si/cm²), a slight defect reduction occurred to a depth of ~ 100 nm in the near surface region after 500 °C. Further annealing at higher temperatures lead to reduction in the damage plateau width, starting from the sample bulk. The latter effect could be attributed to the solid-phase regrowth of the β -phase from the bulk¹⁷.

Figure 4 shows diffractograms from the same samples at all stages in the annealing series. For the lowest implantation fluence, a shoulder peak appeared at 38.25° (2.35 Å) after implantation. This peak was attributed to implantation-induced strain. For the intermediate fluence, similar strain effects were present in the diffractograms, in addition to the peak labelled as B, emerging around 37.7 degrees (2.38 Å). After annealing at 700 °C, this peak disappeared, approximately coinciding with a reduction of the defect levels observed in RBS/c. For the highest implantation fluence, a double peak appeared around 37.7 degrees (2.38 Å), see peaks labeled A and B in the figure. Peak B disappeared after annealing at 700 °C, and peak A underwent a minor shift towards smaller angles with increasing annealing temperature. For temperatures in excess of 700 °C, a diffraction peak appeared around 37.3 degrees (2.41 Å), labeled D, with increasing peak intensity for increased annealing temperatures. This diffraction peak was attributed to regrowth of β - Ga_2O_3 , with the peak corresponding to diffraction from (310)-planes²³. After annealing at 1200 °C, an additional narrow diffraction peak, labeled as peak E, appeared at 37.4 degrees (2.40 Å). This peak disappeared after annealing at 1300 °C.

Potentially, peaks B and A can be assigned to κ -(210) and κ -(131) planes, following the identification suggested previously¹⁷. With this assignment, an isotropic compressive strain of 1.8 % would be required to match the data from the as-implanted sample to literature references³. Hence, if the additional diffraction peaks are due to κ - Ga_2O_3 , then there is substantial strain in the samples after implantation. Similarly, it is possible to attribute peak A to the (310) diffraction peak of β - Ga_2O_3 and peak B to the (401) diffraction peak. This assignment gives a compressive strain of 0.92% and 0.68% respectively, assuming isotropic strain and taking literature values from the work by Åhman et al.²³. However, literature results suggest a peak intensity ratio of 55 for the (401) and (310) peaks, while our diffractograms give an intensity ratio of 3 between peaks B and A. Thus, the XRD data in Figure 2 and Figure 4 were insufficient to unambiguously identify the origin of peaks A and B.

For the intermediate implantation fluence, another weak diffraction peak appeared at 38.16° (2.356 Å) after annealing at 1200 °C. For the highest implantation fluence, a straight shoulder appeared at 38.22° (2.353 Å) after annealing at 1100 °C. These features in the diffractogram appear near the (411) diffraction peak from δ - Ga_2O_3 at 38.2° (2.36 Å)⁷. Thus, presence of a slightly strained δ -phase in our samples is possible. However, since we did not observe a consistent

contribution from this diffraction peak, its origins were not investigated further. Similarly, the origins of peak E were not investigated, since it occurred in only one of the diffractograms.

3.3 Defect microstructure

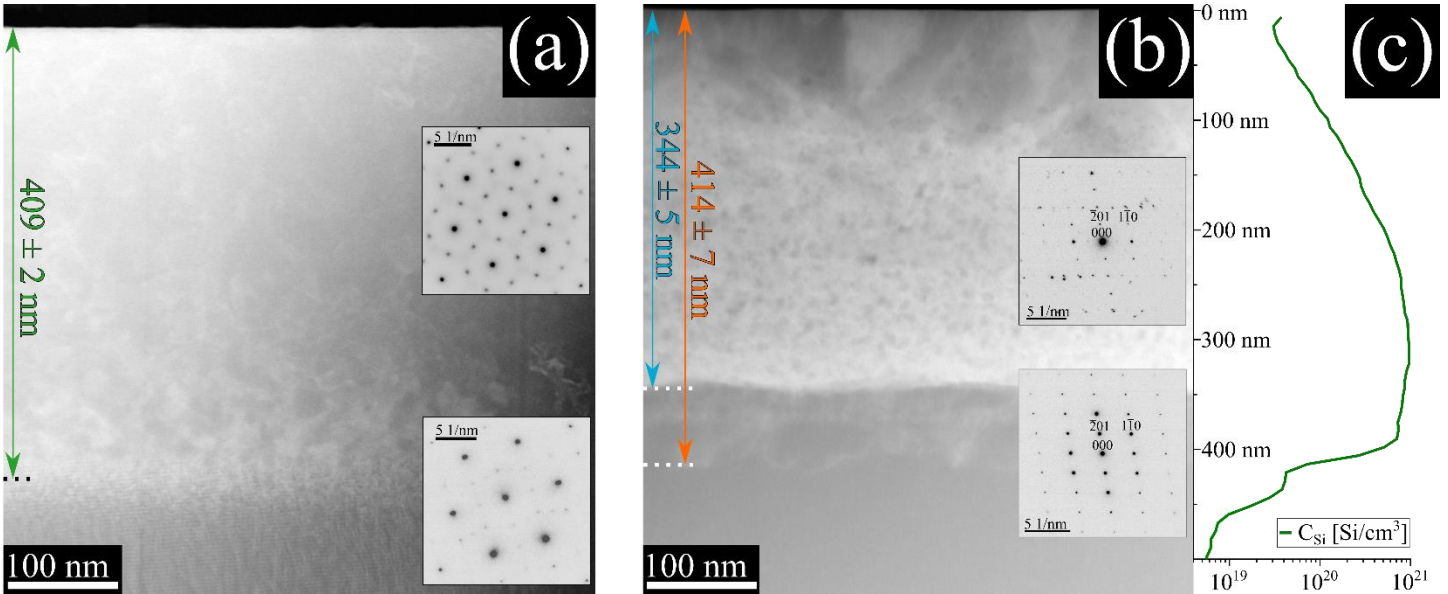


Figure 5 STEM ADF images from a) an as-implanted $(\bar{2}01)$ -oriented sample with implantation fluence 2×10^{16} Si/cm² and b) a $(\bar{2}01)$ -oriented sample implanted to the same fluence and annealed at 1100 °C. Colored arrows and numbers mark relevant depth measurements from the samples. Insets show diffraction patterns from the implanted layer (upper inset) and bulk (lower inset). c) Secondary ion mass spectrometry (SIMS) profile of the Si-concentration in units of atoms/cm³, acquired from a circular area with diameter 33 μ m. The vertical length scale is shared between b) and c).

To further investigate the microstructure of the samples, we proceeded to study $(\bar{2}01)$ -oriented samples implanted to high fluence (2×10^{16} Si/cm²) both before and after annealing (1100 °C, 30 minutes) in more detail. Figure 5 shows STEM annular dark field (ADF) images of the near-surface region of the two samples in panels a) and b), respectively. SAD patterns from the implanted layer and the underlying bulk have been included as insets.

The ADF images in Figure 5 reveal a contrast variation, with a bright contrast region extending from the surface to the depth of ~ 400 and ~ 340 nm, in panels a) and b), respectively. The bright contrast is attributed to increased strain values. The colored arrows in Figure 5 indicate three characteristic depths in the samples, with average values and uncertainties acquired from 10 measurements at different positions. In the as-implanted sample, the depth of the bright-contrast layer was measured to be 409 ± 2 nm (green arrow), while the corresponding depth in the annealed sample was found to be 344 ± 5 nm (blue arrow). Some residual streaks of bright contrast remained in the annealed sample and extended to a depth of 414 ± 7 nm (orange arrow) which was consistent with the observed depth of the damaged layer in the as-implanted sample. This indicated that the region in which these streaks were observed represents an area where crystal regrowth from the bulk had occurred. The width of the bright contrast band was reduced from 409 nm to 344 nm after annealing at 1100 °C, a reduction of 65 nm. Inspection of the RBS/c spectra showed that both the absolute depth values and the changes are comparable with the evolution of the defect plateau for a sample with the same implantation fluence (2×10^{16} Si/cm²).

Figure 5b) features lateral contrast variations in the upper 100 nm of the sample. This contrast variation corresponded to the regrowth of β -Ga₂O₃. From the ADF contrast, which is sensitive to diffraction, the granular structure of the regrown β -phase is apparent. RBS/c spectra from the sample with the same fluence (2×10^{16} Si/cm²) also revealed reduced disorder near the sample surface after annealing. This damage reduction in the near-surface region occurred for the comparatively low annealing temperature of 500 °C, suggesting that regrowth of the β -phase near the sample surface started at comparatively low annealing temperatures. However, we did not observe continuation of the regrowth from the surface beyond the upper 100 nm of the sample even after annealing at 1100 °C.

The insets in Figure 5 show SAD patterns from the implanted layer and the underlying bulk for as-implanted and annealed samples. The diffraction pattern from the implanted layer in the as-implanted sample displayed hexagonal symmetry, in accordance with that reported previously^{17,21}, with weak diffraction spots and low-intensity bands between the strongest reflections. The work by Cora et al. has also shown hexagonal symmetry for diffraction measurements of κ -Ga₂O₃³. However, the plane spacings in our SAD patterns deviated from the plane spacings in the relaxed κ -Ga₂O₃. Additionally, the low-intensity features in the diffraction patterns were not fully consistent with those reported by Cora et al.³. However, and importantly, the SAD pattern in Figure 5a) is obviously different from that of β -Ga₂O₃. Firstly, it does not match the plane spacings reported in literature²³. Secondly, its structure does not match the SAD pattern from the unimplanted bulk in the same sample. Thus, it is clear that ion implantation lead to structural transformation in the implanted layer, consistently with literature^{17,21}. This warrants a thorough investigation of the structure and its dependencies on the implanted specie, sample orientation and structural changes during thermal treatments, but is considered outside the scope of the present study.

The SAD pattern from the implanted layer in the annealed sample revealed diffraction spots corresponding to β -Ga₂O₃. It should be noted that as compared to the SAD pattern from the unimplanted bulk areas, composed of highly ordered single crystal β -Ga₂O₃, the SAD pattern from the implanted layer is more complex due to a granular crystal structure, tilted grains, defects and Moiré fringes. However, we did not observe contributions from other phases or polymorphs. For the sample implanted to the same fluence (2×10^{16} Si/cm²) and annealed at the same temperature (1100 °C), RBS/c results also revealed high remaining disorder levels. Therefore, it was expected that the implanted layer should contain many defects even after anneals at 1100 °C.

The secondary ion mass spectrometry (SIMS) profile of the annealed sample in Figure 5c) reveals an abrupt Si-concentration decrease at ~400 nm. This value is close to the observed depth of the damaged layer in the as-implanted sample (409 nm). Consequently, the SIMS results indicate that diffusion of Si into the sample bulk is suppressed for annealing at 1100 °C.

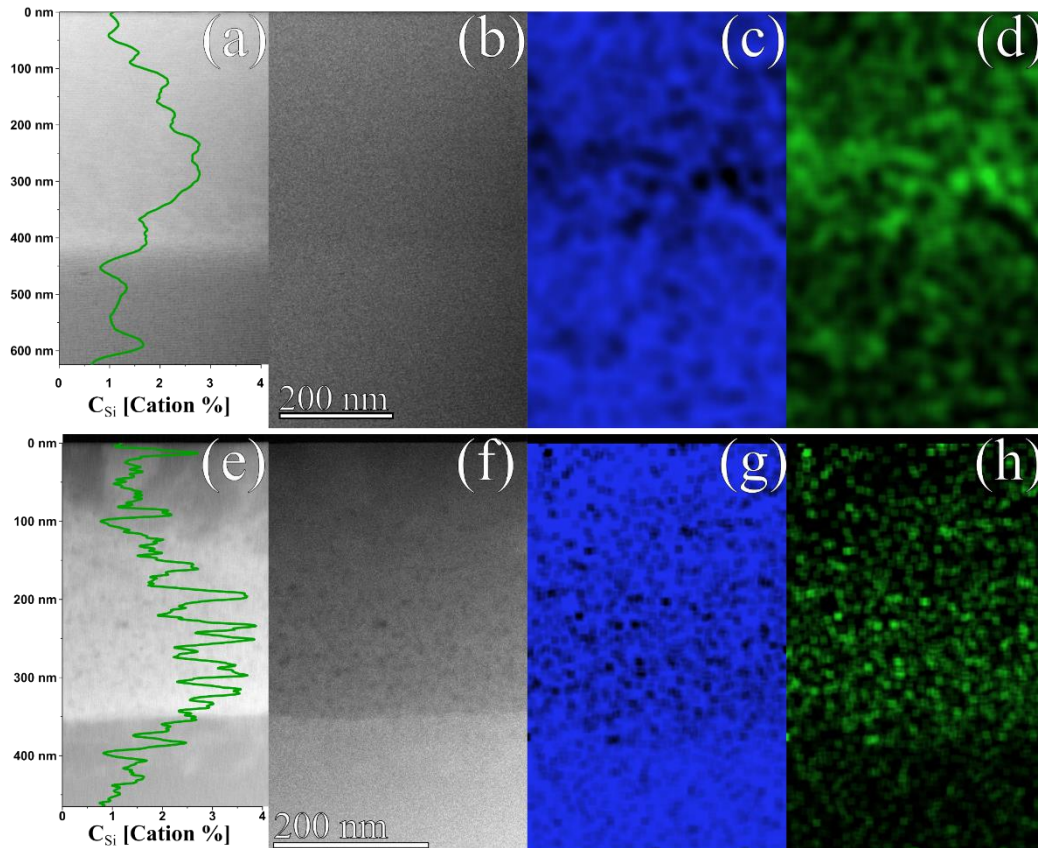


Figure 6 a) STEM ADF, b) HAADF and EDS maps for c) Ga and d) Si for the as-implanted sample with fluence 2×10^{16} Si/cm². The Si concentration profile, in units of cation (atomic) percent, is superposed on the ADF image. The scalebar is given in the HAADF image, and is shared across all images. Corresponding datasets for a sample annealed at 1100 °C are shown in subfigures e)-h).

Further, the chemical compositional variations in the sample implanted with 2×10^{16} Si/cm² were investigated using EDS in STEM. Figure 6 shows the EDS data from the as-implanted and annealed samples. The silicon concentration plots show a maximum Si-concentration around 250 nm below the sample surface for the as-implanted sample, consistent with expected values from SRIM calculations (see ion ranges in Figure 1).

In the annealed sample, the concentration profile revealed the Gaussian-like implantation profile expected from SRIM (Figure 6e)), with a peak in the Si-concentration around 250-300 nm. In addition, there were oscillations in the Si-concentration over length scales of 10-20 nm. The corresponding EDS maps (Figure 6g) and h)) showed areas with increased Si-concentration and decreased Ga-concentration. This accumulation of the implanted silicon atoms was not seen in the as-implanted sample, although there was a slight depletion of Ga near the implantation peak. The results show that annealing of the sample lead to the formation of Si-rich particles. The corresponding high-angle annular dark field (HAADF) image revealed areas with dark contrast, which coincided with Si-accumulation for many of the areas. However, some of the dark areas in HAADF did not coincide with Si-accumulation. Consequently, some of the dark areas in the HAADF image were not caused by Si-rich particles. A plausible explanation for these additional dark-contrast areas in the HAADF image is formation of voids in the sample, which would lead to reduced mass-thickness contrast.

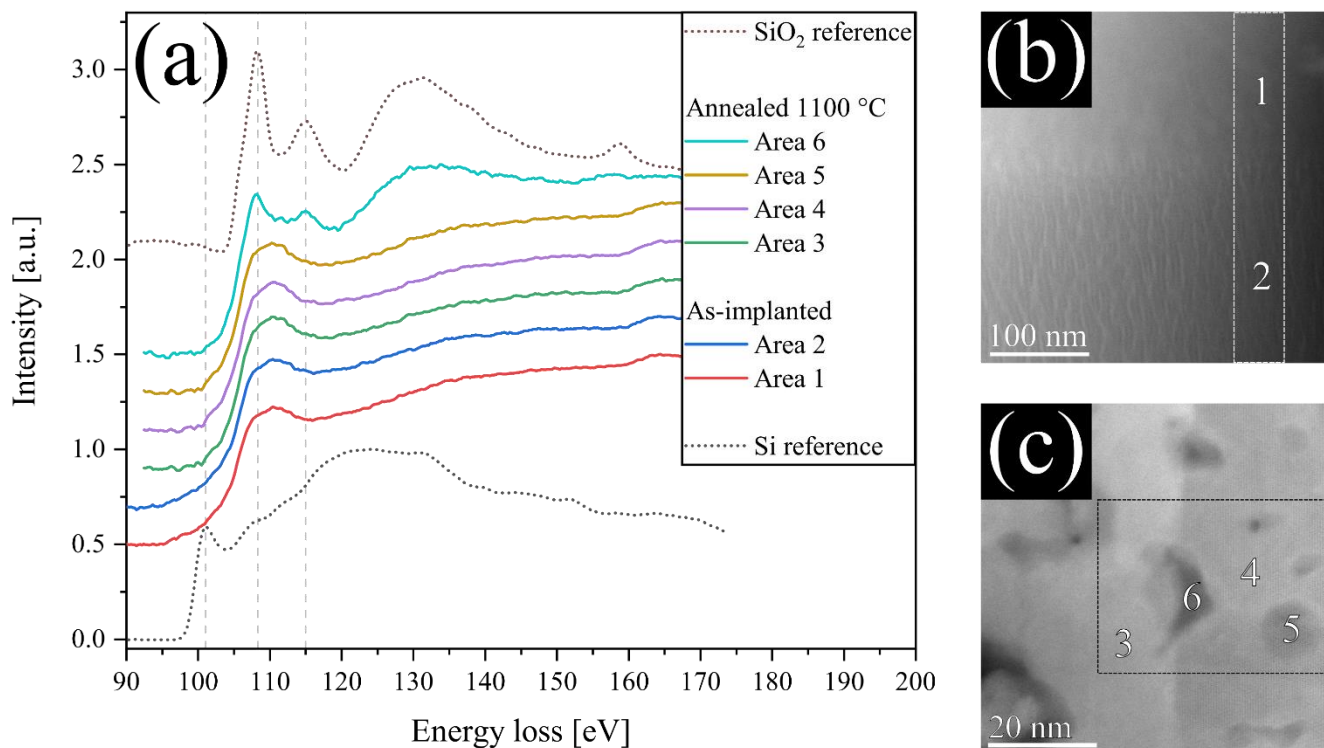


Figure 7 a) Core-loss EELS spectra of the Si $L_{2,3}$ edge of the implanted layer and the bulk in an as-implanted sample (implantation fluence 2×10^{16} Si/cm^2) and four selected areas in a sample annealed at 1100°C (implantation fluence 2×10^{16} Si/cm^2). Reference EELS spectra from Si and SiO_2 in dotted lines are included for comparison (see the text for references). The labeling corresponds to the regions of acquisition indicated by white numbers in ADF images from b) the as-implanted sample and c) the annealed sample. Dashed lines in images indicate the region of interest for EELS measurements.

EELS measurements were performed to identify the composition of the Si-rich particles revealed by the EDS measurements on the annealed sample and additionally to reveal chemical changes in the surroundings of Si between samples. Figure 7 shows EELS data from the same samples as investigated in Figure 5 and Figure 6, i.e. ($\bar{2}01$)-oriented samples implanted with 2×10^{16} Si/cm^2 , as-implanted and annealed at 1100°C . In addition, reference spectra from crystalline Si and amorphous silicon dioxide are included^{26,27}. The spectra revealed a change in the Si $L_{2,3}$ -edge lineshape in one of the dark contrast regions (area 6) in the ADF image from the annealed sample (Figure 7c)). In the EELS spectrum from area 6, the L-edge lineshape was consistent with previously reported results from silicon dioxide^{26,28,29}. Hence, EELS results indicate that the Si-accumulation observed in EDS was likely due to the formation of SiO_2 particles during annealing. The formation of such particles could contribute to the suppression of Si diffusion which was observed in the SIMS profile from the same sample.

The EELS data from the different regions of both samples not showing signs of particle or void formation (Figure 7a), spectra from areas 1-4) and one of the other dark areas in ADF images (spectrum from area 5) displayed a comparatively broad peak near the onset, and did not show the secondary peak around 115 eV, which was clearly visible in the spectrum from area 6 and the SiO_2 reference spectrum. Therefore, EELS data did not show presence of SiO_2 in areas 1-5. Instead, the origin of the EELS signal from these areas was interpreted in terms of substitutional Si on Ga sites (Si_{Ga}) or interstitial Si (Si_i) in $\beta\text{-Ga}_2\text{O}_3$. The latter option is unlikely to dominate due to the higher formation energy of Si_i compared with Si_{Ga} in $\beta\text{-Ga}_2\text{O}_3$ ¹² and the high density of vacancies produced during ion implantation into which Si could migrate to form Si_{Ga} . It has been previously reported that Si prefers the tetrahedral Ga(I) site in Ga_2O_3 ³⁰, so it is likely that the major contributor to this signal was from Si_{Ga} situated on tetrahedral Ga(I) sites. Since the Si $L_{2,3}$ -edge onset occurred at the same energy for all the spectra from areas 1-5, it is likely that the local surroundings of Si were similar in all of these areas.

In the present study, most attention has been paid to damage accumulation and annealing behavior in ($\bar{2}01$)-oriented samples. Normally, generation of similar defects and defect concentrations should be expected for implantation into differently oriented samples, such as the (010)- and (001)-oriented samples which were investigated in the surface orientation study. However, since β -Ga₂O₃ is highly anisotropic, certain differences may exist. For instance, the crystal regrowth from the bulk which was observed in RBS/c and (S)TEM may occur at different rates for different crystallographic orientations.

Conclusion

In conclusion, we have studied defect accumulation and annealing phenomena in Si-implanted β -Ga₂O₃ wafers, having ($\bar{2}01$), (010), and (001) orientations, employing a combination of RBS/c, XRD, and (S)TEM. This systematic approach allowed us to investigate complex structural transformations occurring in Si-implanted β -Ga₂O₃ as a function of the sample orientation, accumulated fluence and annealing temperature. In as-implanted samples, interesting disorder accumulation kinetics consistent with the literature was observed. In particular, the RBS/c, XRD, and (S)TEM data combined, suggested that the radiation disorder buildup in Si-implanted β -Ga₂O₃ is accompanied by significant strain accumulation, which assists crystalline-to-crystalline structural transformations instead of amorphization. The analysis of the annealed samples suggested complex structural transformations which occurred as a function of the fluence and temperature. Moreover, a detailed (S)TEM analysis of the sample implanted with 2×10^{16} Si/cm² and annealed at 1100 °C was enhanced by applying EDS and EELS. EDS analysis unveiled Si agglomerations of size 10-20 nm, and EELS revealed that the agglomerations were composed of silicon dioxide. The Si signal was also observed outside of the agglomerations, likely occurring as substitutional Si on Ga sites.

Acknowledgements

The Research Council of Norway is acknowledged for the support to the Norwegian Micro- and Nano-Fabrication Facility, NorFab, project number 295864, and the Norwegian Center for Transmission Electron Microscopy, NORTEM, project number 197405, and for support to the project Functionalization of Conducting Oxides by Ion beam and defect engineering, project number 287729. The INTPART Program at the Research Council of Norway, projects nr 26/574 and 322382 enabled the international collaborations. Part of the experiments were realized at the CANAM (Centre of Accelerators and Nuclear Analytical Methods) infrastructure LM 2015056 and under the project CANAM OP, CZ.02.1.01/0.0/0.0/16_013/0001812 supported by MEYS of the Czech Republic.

References

- ¹ M. Zinkevich and F. Aldinger, *J. Am. Ceram. Soc.* **87**, 683 (2004).
- ² H.Y. Playford, A.C. Hannon, E.R. Barney, and R.I. Walton, *Chem. - A Eur. J.* **19**, 2803 (2013).
- ³ I. Cora, F. Mezzadri, F. Boschi, M. Bosi, M. Čaplovičová, G. Calestani, I. Dódony, B. Pécz, and R. Fornari, *CrystEngComm* **19**, 1509 (2017).
- ⁴ D. Shinohara and S. Fujita, *Jpn. J. Appl. Phys.* **47**, 7311 (2008).
- ⁵ V. Gottschalch, S. Merker, S. Blaurock, M. Kneiß, U. Teschner, M. Grundmann, and H. Krautscheid, *J. Cryst. Growth* **510**, 76 (2019).
- ⁶ S. Yoshioka, H. Hayashi, A. Kuwabara, F. Oba, K. Matsunaga, and I. Tanaka, *J. Phys. Condens. Matter* **19**, 346211 (2007).
- ⁷ R. Roy, V.G. Hill, and E.F. Osborn, *J. Am. Chem. Soc.* **74**, 719 (1952).
- ⁸ R. Fornari, M. Pavesi, V. Montedoro, D. Klimm, F. Mezzadri, I. Cora, B. Pécz, F. Boschi, A. Parisini, A. Baraldi, C. Ferrari, E. Gombia, and M. Bosi, *Acta Mater.* **140**, 411 (2017).
- ⁹ I. Cora, Zs. Fogarassy, R. Fornari, M. Bosi, A. Rečnik, and B. Pécz, *Acta Mater.* **183**, 216 (2020).
- ¹⁰ Y. Xu, J.-H. Park, Z. Yao, C. Wolverton, M. Razeghi, J. Wu, and V.P. Dravid, *ACS Appl. Mater. Interfaces* **11**, 5536 (2019).

- ¹¹ H. Sun, K.-H. Li, C.G.T. Castanedo, S. Okur, G.S. Tompa, T. Salagaj, S. Lopatin, A. Genovese, and X. Li, *Cryst. Growth Des.* **18**, 2370 (2018).
- ¹² A. Bouzid and A. Pasquarello, *Phys. Status Solidi - Rapid Res. Lett.* **13**, 1800633 (2019).
- ¹³ T. Zheng, Q. Wang, J. Dang, W. He, L. Wang, and S. Zheng, *Comput. Mater. Sci.* **174**, 109505 (2020).
- ¹⁴ E.G. Villora, K. Shimamura, Y. Yoshikawa, T. Ujiie, and K. Aoki, *Appl. Phys. Lett.* **92**, 202120 (2008).
- ¹⁵ K. Sasaki, M. Higashiwaki, A. Kuramata, T. Masui, and S. Yamakoshi, *Appl. Phys. Express* **6**, 086502 (2013).
- ¹⁶ A. Azarov, V. Venkatachalapathy, L. Vines, E. Monakhov, I.-H. Lee, and A. Kuznetsov, *Appl. Phys. Lett.* **119**, 182103 (2021).
- ¹⁷ A. Azarov, C. Bazioti, V. Venkatachalapathy, P. Vajeeston, E. Monakhov, and A. Kuznetsov, *Phys. Rev. Lett.* **128**, 015704 (2022).
- ¹⁸ E. Wendler, E. Treiber, J. Baldauf, S. Wolf, and C. Ronning, *Nucl. Instruments Methods Phys. Res. Sect. B Beam Interact. with Mater. Atoms* **379**, 85 (2016).
- ¹⁹ M. Peres, K. Lorenz, E. Alves, E. Nogales, B. Méndez, X. Biquard, B. Daudin, E.G. Villora, and K. Shimamura, *J. Phys. D: Appl. Phys.* **50**, 325101 (2017).
- ²⁰ A. Azarov, V. Venkatachalapathy, E. V. Monakhov, and A.Y. Kuznetsov, *Appl. Phys. Lett.* **118**, 232101 (2021).
- ²¹ E.A. Anber, D. Foley, A.C. Lang, J. Nathaniel, J.L. Hart, M.J. Tadjer, K.D. Hobart, S. Pearton, and M.L. Taheri, *Appl. Phys. Lett.* **117**, 152101 (2020).
- ²² J.F. Ziegler, M.D. Ziegler, and J.P. Biersack, *Nucl. Instruments Methods Phys. Res. Sect. B Beam Interact. with Mater. Atoms* **268**, 1818 (2010).
- ²³ J. Åhman, G. Svensson, and J. Albertsson, *Acta Crystallogr. Sect. C Cryst. Struct. Commun.* **52**, 1336 (1996).
- ²⁴ R. Sugie, T. Uchida, A. Hashimoto, S. Akahori, K. Matsumura, and Y. Tanii, *Appl. Phys. Express* **13**, 126502 (2020).
- ²⁵ A. Tuross, P. Jóźwik, M. Wójcik, J. Gaca, R. Ratajczak, and A. Stonert, *Acta Mater.* **134**, 249 (2017).
- ²⁶ P.E. Batson, *Microsc. Microanal. Microstruct.* **2**, 395 (1991).
- ²⁷ P. Ewels, T. Sikora, V. Serin, C.P. Ewels, and L. Lajaunie, *Microsc. Microanal.* **22**, 717 (2016).
- ²⁸ T. Zheleva, A. Lelis, G. Duscher, F. Liu, I. Levin, and M. Das, *Appl. Phys. Lett.* **93**, 022108 (2008).
- ²⁹ G. Kissinger, M.A. Schubert, D. Kot, and T. Grabolla, *ECS J. Solid State Sci. Technol.* **6**, N54 (2017).
- ³⁰ S. Lany, *APL Mater.* **6**, 046103 (2018).